

Check for updates



RESEARCH ARTICLE OPEN ACCESS

Enhanced Structural Transformation Enabled by Low-Crystalline Vanadium Oxides in Aqueous Zinc-Ion Batteries

Hyeonjun Lee¹ | Hyungjin Lee² | Sangki Lee¹ | Hyojun Lim³ | Seung-Tae Hong^{2,4} | Hyung Do Kim⁵ D | Munseok S. Chae¹ D

¹Department of Nanotechnology Engineering, Pukyong National University, Busan, Republic of Korea | ²Department of Energy Science and Engineering, DGIST, Daegu, Republic of Korea | ³Department of Nuclear Science and Engineering, Massachusetts Institute of Technology, Cambridge, Massachusetts, USA | ⁴Department of Chemistry and Chemical Biology, University of New Mexico, Albuquerque, New Mexico, USA | ⁵Department of Polymer Chemistry, Graduate School of Engineering, Kyoto University, Kyoto, Japan

Correspondence: Hyung Do Kim (hyungdokim@photo.polym.kyoto-u.ac.jp) | Munseok S. Chae (mschae@pknu.ac.kr)

Received: 26 March 2025 | Revised: 16 June 2025 | Accepted: 23 June 2025

Funding: This work was partly supported by the Global Joint Research Program funded by Pukyong National University (202411790001) and JSPS KAKENHI Grant No. JP22K14726.

Keywords: aqueous electrolytes materials | cathode materials | low crystalline | V2O5 | zinc-ion batteries

ABSTRACT

Aqueous batteries are gaining attention owing to their high safety and cost-effectiveness. Among these, Zn-based aqueous batteries excel because of Zn's low redox potential ($-0.76\,\mathrm{V}$ vs. SHE), its abundance, and eco-friendliness. However, despite their advantages, challenges, such as low energy density and limited cycle life limit their usage. This study addresses these issues by employing low-crystalline $V_2O_{4.86}$ as a cathode material, enhanced with oxygen vacancies created by controlled annealing time. The structure of low-crystalline $V_2O_{4.86}$ facilitates rapid structural transformation into the highly active phase $Zn_{3+x}(OH)_2V_2O_7$ ·2(H_2O). Electrochemical tests revealed a 22% capacity improvement for low-crystalline $V_2O_{4.86}$ (360 mAh g⁻¹) over high-crystalline V_2O_5 (295 mAh g⁻¹) at 0.8 A g⁻¹, attributed to the presence of active oxygen vacancies. Comprehensive structural analysis, spectroscopy, and diffusion path/barrier studies elucidate the underlying mechanisms for the first time, highlighting the potential of oxygen-engineered V_2O_5 . These findings indicate that electrodes engineered with oxygen vacancies offer promising insights in advancing cathode materials for high-performance secondary battery technologies.

1 | Introduction

In recent years, rechargeable batteries have received significant attention for their ability to meet the growing demands of electric vehicles, portable electronic devices, and energy storage systems. Among the various battery technologies, lithium-ion batteries (LIBs) have dominated the market owing to their high operating voltage and superior energy density [1]. However, LIBs usage is not without its challenges, including safety concerns related to flammability and high costs stemming from the uneven distribution of lithium resources. These limitations have

driven extensive research into next-generation battery technologies.

Multivalent ion rechargeable batteries, utilizing elements such as Al [2], Ca [3], Mg [4–6], Zn [7–9], and Mn [10–12], have emerged as promising alternatives. These systems offer several advantages, including high energy density, low cost due to the elemental abundance of raw materials, and improved safety features. Among these candidates, Zn has garnered particular interest owing to its exceptional properties, inclusive of a high theoretical capacity (820 mAh g $^{-1}$), widespread natural

This is an open access article under the terms of the Creative Commons Attribution License, which permits use, distribution and reproduction in any medium, provided the original work is properly cited.

© 2025 The Author(s). Battery Energy published by Xijing University and John Wiley & Sons Australia, Ltd.

availability, low production costs, and environmental friendliness [13].

Aqueous zinc-ion batteries (ZIBs) have emerged as a particularly attractive energy storage technology because of their excellent electrochemical stability, extended operational lifespan, and economic feasibility. Additionally, the aqueous system offers distinct advantages such as nonflammability, cost-effectiveness, and suitability for large-scale energy storage applications, making it an ideal candidate for next-generation energy solutions.

To enhance the performance of ZIBs, extensive research efforts have been devoted to exploring various cathode materials, including manganese oxides [14–16], phosphate-based materials [17, 18], and vanadium oxides [19, 20]. Manganese oxides, despite showing potential, undergo protonation during electrochemical reactions, leading to structural transformations and subsequent manganese dissolution, which significantly compromises cycling stability [21]. In contrast, vanadium-based oxides utilize intercalation mechanisms, offering enhanced cycling stability and high capacities. However, despite these benefits, studies on vanadium-based materials remain relatively scarce and have primarily focused on the conventional V_2O_5 structure and its various polymorphs [22].

Among the polymorphs of V_2O_5 , the α - V_2O_5 structure is the simplest to synthesize and employ [23]. However, in zinc aqueous solutions, α - V_2O_5 undergoes a phase transformation into $Zn_3(OH)_2V_2O_7\cdot 2(H_2O)$, facilitating reversible operation [24–26]. This transformation is associated with a capacity activation process that necessitates considerable time and cycling to fully develop. To address this limitation and enhance both activation efficiency and electrochemical performance, structural engineering of V_2O_5 is critical.

In particular, we hypothesize that oxygen defects in V_2O_5 and the corresponding differences in crystallinity can significantly influence electrochemical activation [27]. As illustrated in Figure 1a, highly crystalline V_2O_5 features straight one-dimensional cation tunnels, which limit reaction flexibility. In contrast, low-crystalline V_2O_5 exhibits structural twisting, higher vacancy density, and more unstable states, which are likely to promote highly active reaction sites. Moreover, the introduction of a three-dimensional framework, rather than a one-dimensional tunnel structure, is expected to further enhance electrochemical performance by enabling better ionic transport and improved output.

In this study, we demonstrate the superior performance of ZIBs using low-crystalline vanadium oxide with oxygen vacancies as the cathode material. The distinctions between low- and high-crystallinity vanadium oxides were comprehensively analyzed through a combination of crystallographic studies, electrochemical characterizations, spectroscopic analyses, and diffusion pathway calculations. The low-crystalline V_2O_5 structure exhibits superior electrochemical performance, including higher capacity, improved rate capability, and enhanced cycling stability. Notably, the introduction of oxygen vacancies within the vanadium oxide structure not only creates additional diffusion pathways but also accelerates the structural

transformation into the $\rm Zn_3(OH)_2V_2O_7\cdot 2(H_2O)$ phase, significantly boosting overall electrochemical performance. In addition, this study elucidates the detailed reaction phenomena for the first time. These findings offer compelling evidence that structural engineering can activate host structures, opening new possibilities for optimizing other host materials in energy storage applications.

2 | Experimental Methods

2.1 | Material Synthesis

A sol–gel synthesis method was used to prepare V_2O_5 [28]. Briefly, 1 M V_2O_5 (\geq 99%, Sigma-Aldrich) and 6 M oxalic acid (\geq 99%, Thermo Fisher Scientific) were dissolved in a beaker containing 350 mL of deionized water. The suspension was stirred vigorously at 90°C for 12 h, gradually forming a blue solution. After drying, the gel powder was hand-ground and then heated at 400°C for 1 and 4 h to obtain low- and high-crystalline V_2O_5 , respectively. Finally, the as-synthesized powders were hand-ground again.

2.2 | Material Characterization

The size of the crystals varied depending on the synthesis time. Detailed differences are provided in the Supporting Information. To analyze purity and morphology, the as-synthesized powder was examined using X-ray diffraction (XRD; Rigaku Mini-Flex 600, with Cu K α radiation, $\lambda = 1.5418$ Å), scanning electron microscopy (SEM; Hitachi SU-8020), and transmission electron microscopy (TEM; Hitachi/HF-3300). Compared with previous studies, these analyses confirmed that the synthesis was successful.

2.3 | Electrochemical Characterization

All electrochemical performances were evaluated using the EC-Lab software with a VMP-3e multichannel potentiostat (Biologic Science Instruments SAS). Cyclic voltammetry (CV), galvanostatic discharge/charge, and impedance spectroscopy were employed to assess the electrochemical performance.

As-prepared high-crystalline and low-crystalline V_2O_5 were utilized as a cathode, and the 1 M $\rm Zn(ClO_4)_2$ aqueous solution was utilized as an electrolyte. Additionally, Zn foil and rod were utilized as the anode and reference electrodes, respectively.

The cathode electrode was prepared using V_2O_5 synthesized in the study, conductive carbon (Super P, Timcal), and poly (vinylidene fluoride) (PVDF; Kureha Co.) dissolved in N-methyl-2-pyrrolidone (NMP) solution in a weight ratio of 7:2:1. It was homogenized using a THINKY mixer at 1500 rpm for 20 min. After repeating the process once again, the resulting mixture was uniformly coated onto a stainless steel (SS 316L, 20 μm) foil and dried in an oven at 70°C for 12 h. After removing the NMP solvent, the coated electrode was cut into circular pieces with an area of 1.32 cm² using a precision cutter, equipped with a 13π cutting tool. The active material weighed 1.6 mg.

2 of 9 Battery Energy, 2025

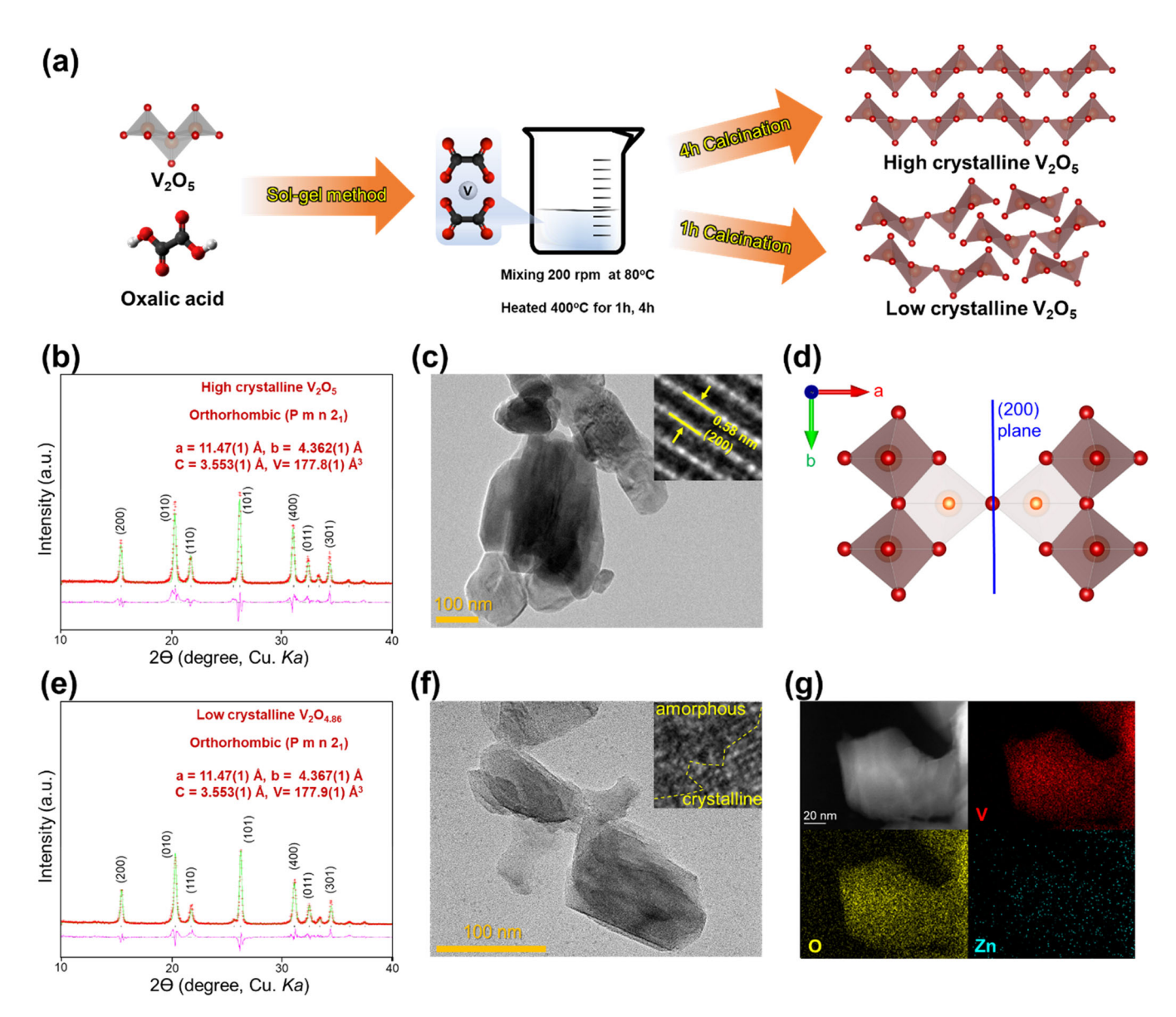


FIGURE 1 (a) Schematic illustration of the synthesis of V_2O_5 sol-gel in 1 and 4 h. XRD profiles of the powder showing the diffraction patterns of high-crystalline V_2O_5 (b) and low-crystalline $V_2O_{4.86}$ (e). (c) TEM image of high-crystalline V_2O_5 , with a high-resolution image inset, showing the well-defined lattice fringes, and (d) its corresponding crystal structure. (f) TEM image of low-crystalline $V_2O_{4.86}$, with a high-resolution image inset, highlighting structural twisting and defects. (g) EDX elemental mapping images of low-crystalline $V_2O_{4.86}$, revealing a homogeneous distribution of vanadium and oxygen atoms.

2.4 | Diffusion Barrier Calculation

The migration barrier calculations for ion diffusion were performed using the BV-GUI program [29, 30], integrating structural data from previously reported studies on V_2O_5 and $Zn_{3+x}(OH)_2V_2O_7\cdot 2(H_2O)$ systems. The three-dimensional diffusion pathways for the ions were graphically visualized using the VESTA software, enabling detailed analysis of migration pathways and energy barriers.

The zinc and proton migration barriers were specifically calculated using the softBV-GUI program, which leverages bond valence-based methods to evaluate ionic migration. These computational approaches provided quantitative insights into the zinc and proton migration mechanisms, highlighting their respective contributions to the electrochemical performance of the V_2O_5 and $Z_{n_{3+x}}(OH)_2V_2O_7\cdot 2(H_2O)$ structures.

3 | Results and Discussion

3.1 | Material Synthesis and Characterizations of High-/Low-Crystalline Vanadium Oxides

High- and low-crystalline vanadium oxides were synthesized via a solid-state method [28]. Initially, V_2O_5 was dissolved in water with oxalic acid, resulting in the formation of oxalic vanadates. The resulting mixture was thoroughly dried to form a gel, which was subsequently annealed at 400° C for different durations: 4 h for high-crystalline V_2O_5 and 1 h for low-crystalline $V_2O_{4.86}$, as depicted in Figure 1a. Prolonged annealing time reduced the number of oxygen vacancies while enhancing crystallinity, thereby improving structural stability. To confirm the synthesized powders, XRD analysis was conducted, and the data were refined using the Rietveld method (Figure 1b,e).

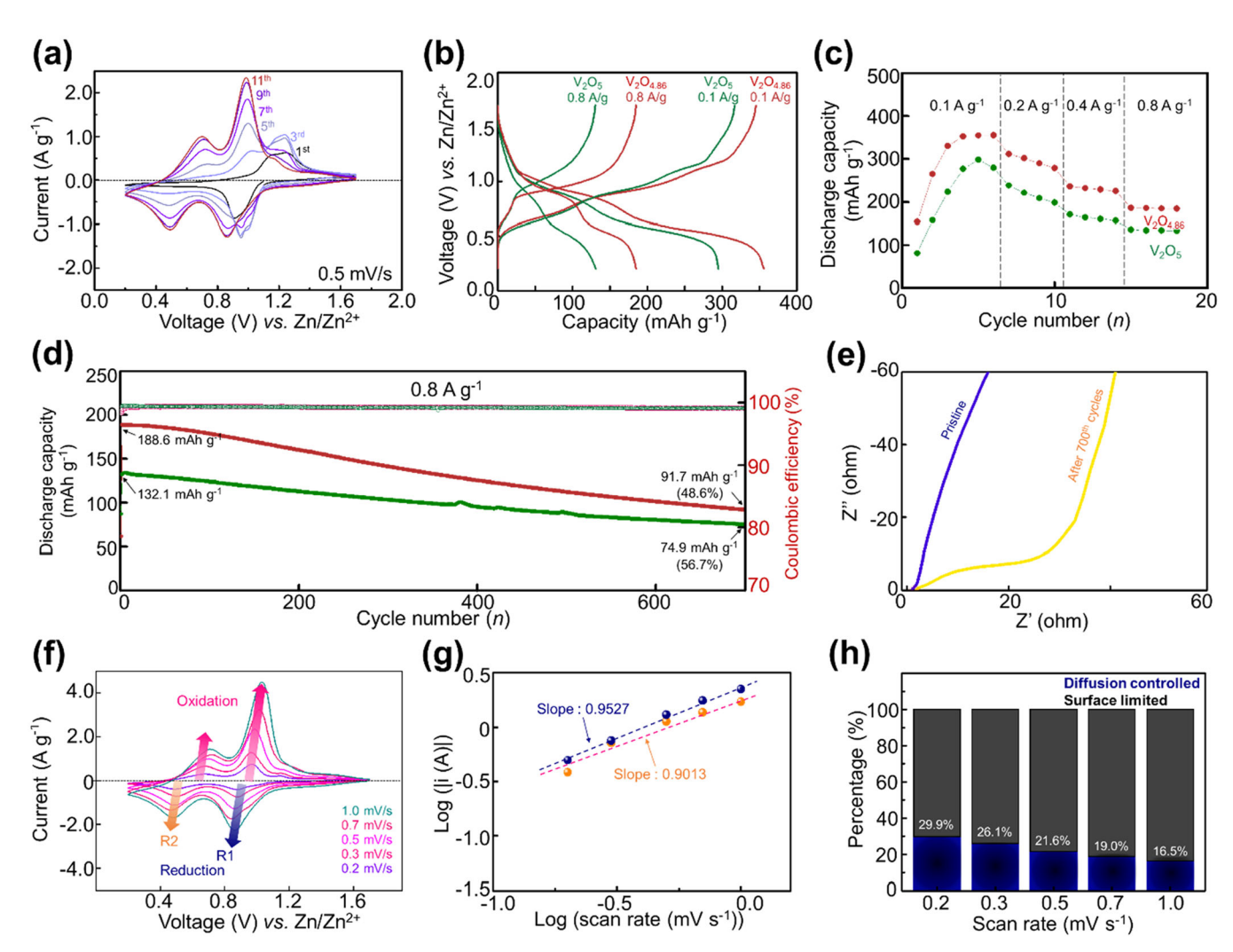


FIGURE 2 | (a) Cyclic voltammetry (CV) curves measured at a scan rate of $0.5 \,\mathrm{mV} \,\mathrm{s}^{-1}$. (b) GCD profiles at current densities of $0.1 \,\mathrm{and} \,0.8 \,\mathrm{Ag}^{-1}$. (c) Rate performance at current densities ranging from $0.1 \,\mathrm{to} \,0.8 \,\mathrm{Ag}^{-1}$. (d) Long-term cycling stability evaluation at a current density of $0.8 \,\mathrm{Ag}^{-1}$. (e) EIS spectra for pristine samples and those after 700 cycles for low-crystalline $V_2O_{4.86}$. (f) CV curves measured at scan rates from $0.2 \,\mathrm{to} \,1.0 \,\mathrm{mV} \,\mathrm{s}^{-1}$. (g) Calculation of b-values based on the relationship between specific cathodic peak current and scan rate. (h) Estimation of the ratios of surface-limited and diffusion-controlled ion reactions of $V_2O_{4.86}$.

The high-crystalline V_2O_5 exhibited sharp and well-defined XRD peaks, indicating high crystallinity, while the low-crystalline $V_2O_{4.86}$ displayed broader peaks, reflecting its reduced crystallinity (Figure S1). In addition, crystallite size calculations further support this observation, with the low-crystalline sample showing an average size of 31.5 nm, while the highly crystalline sample exhibited a size of 41.9 nm (Table S3). Interestingly, although both materials had similar unit cell parameters, Rietveld analysis revealed that the low-crystalline $V_2O_{4.86}$ contained ~0.14 M of small oxygen vacancies. Detailed refinement parameters are listed in Tables S1 and S2.

Electron paramagnetic resonance (EPR) measurements were carried out to confirm the presence of oxygen vacancies. The low-crystalline $V_2O_{4.86}$ sample exhibited a pronounced signal at $g \approx 1.98$, indicative of oxygen vacancies, whereas the highly crystalline V_2O_5 showed weaker intensity (Figure S2). These findings support the hypothesis that structural defects, particularly oxygen vacancies, play a key role in enhancing electrochemical performance.

TEM images (Figure 1c,f) revealed that high-crystalline V_2O_5 consisted of particles sized between 100 and 500 nm, which were significantly larger than those of low-crystalline $V_2O_{4.86}$ (~100 nm). The high-crystalline V_2O_5 showed a well-ordered atomic arrangement, as evidenced by the d(200) spacing of ~0.58 nm (Figure 1c, inset); the corresponding structures are presented in Figure 1d. In contrast, low-crystalline $V_2O_{4.86}$ exhibited an amorphous structure with partially ordered atomic regions, indicative of higher defect density.

SEM-EDX elemental mapping (Figure 1g) confirmed a uniform distribution of vanadium and oxygen atoms throughout the low-crystalline $V_2O_{4.86}$. Trace zinc signals were detected due to background scattering, while EDX spectra and mapping further validated the absence of impurities in the material. Additional detailed morphological and elemental analyses, including SEM images (Figures S3 and S5), SEM-EDX spectra (Figures S4 and S6), and a wide range of TEM images (Figures S7 and S8) are provided in the Supporting Information for both types of powders.

4 of 9

Battery Energy, 2025

3.2 | Electrochemical Characterizations of High-/Low-Crystalline V_2O_5

All electrochemical characterizations were performed using three-electrode beaker-type cells with zinc metal as both the anode and reference electrodes, and vanadium oxides as the cathode electrode.

The CV curves, recorded at a scan rate of 0.5 mV s⁻¹, revealed a gradual activation process, characterized by distinct peaks corresponding to oxidation and reduction reactions (Figure 2a). After the activation period, two prominent oxidation peaks at 0.7 and 1.0 V, along with two reduction peaks at 0.5 and 0.9 V, were observed, indicating stable redox behavior. The activation process necessitates sufficient time to facilitate the complete structural transformation of V₂O₅ into Zn_{3+x}(OH)₂V₂O₇·2(H₂O). At a relatively high scan rate of 0.5 mV s⁻¹, the associated redox transitions manifest progressively over multiple CV cycles, likely due to limited reaction time. This observation implies that slower scan rates or extended discharge durations are essential to promote full phase evolution. Consistently, cycling at a reduced rate results in a nearly complete structural transformation within the first cycle, as verified by ex situ XRD analysis in Figure 4a. However, the highcrystallinity V₂O₅ structure exhibits a slower activation process, along with lower reduction and oxidation current responses (Figure S9). This indicates that our low-crystalline V₂O_{4.86} facilitates and accelerates the structural transformation of V₂O₅.

The galvanostatic charge-discharge (GCD) profiles (Figure 2b) indicated that low-crystalline V₂O_{4.86} delivered superior capacities of $355.4 \,\mathrm{mAh}\,\mathrm{g}^{-1}$ at $0.1\,\mathrm{A}\,\mathrm{g}^{-1}$ and $185.3\,\mathrm{mAh}\,\mathrm{g}^{-1}$ at 0.8 A g⁻¹, significantly outperforming high-crystalline V₂O₅, which exhibited capacities of 294.8 and 131.2 mAh g⁻¹, respectively. Rate capability tests, conducted at various current densities (0.1, 0.2, 0.4, and 0.8 A g⁻¹), further highlighted the differences in performance (Figure 2c and Figure S10). To be specific, low-crystalline V₂O_{4.86} maintained high capacities across the tested current densities, demonstrating robust electrochemical performance irrespective of the applied current and showcasing its superior adaptability to both low and high current conditions. The long-term cycling stability of highcrystalline V₂O₅ and low-crystalline V₂O_{4.86} was evaluated over 700 cycles at a current density of $0.8 \,\mathrm{A\,g^{-1}}$ (Figure 2d). While low-crystalline V2O4.86 exhibited lower capacity retention of 48.6%, it maintained a higher final capacity of 91.7 mAh g⁻¹ compared with its initial capacity of 185.6 mAh g^{-1} . In contrast, high-crystalline V₂O₅ showed a higher capacity retention of 56.7%, yet its final capacity was lower at 74.9 mAh g⁻¹. These results indicated that low-crystalline V₂O_{4.86} outperformed in absolute capacity despite a slightly faster capacity fade. However, both vanadium-based oxides inherently suffer from vanadium dissolution, which remains a critical challenge. Addressing this issue will be essential for improving long-term cycling stability. Both materials demonstrated high Coulombic efficiency, averaging around 99.4% throughout the 700 cycles,

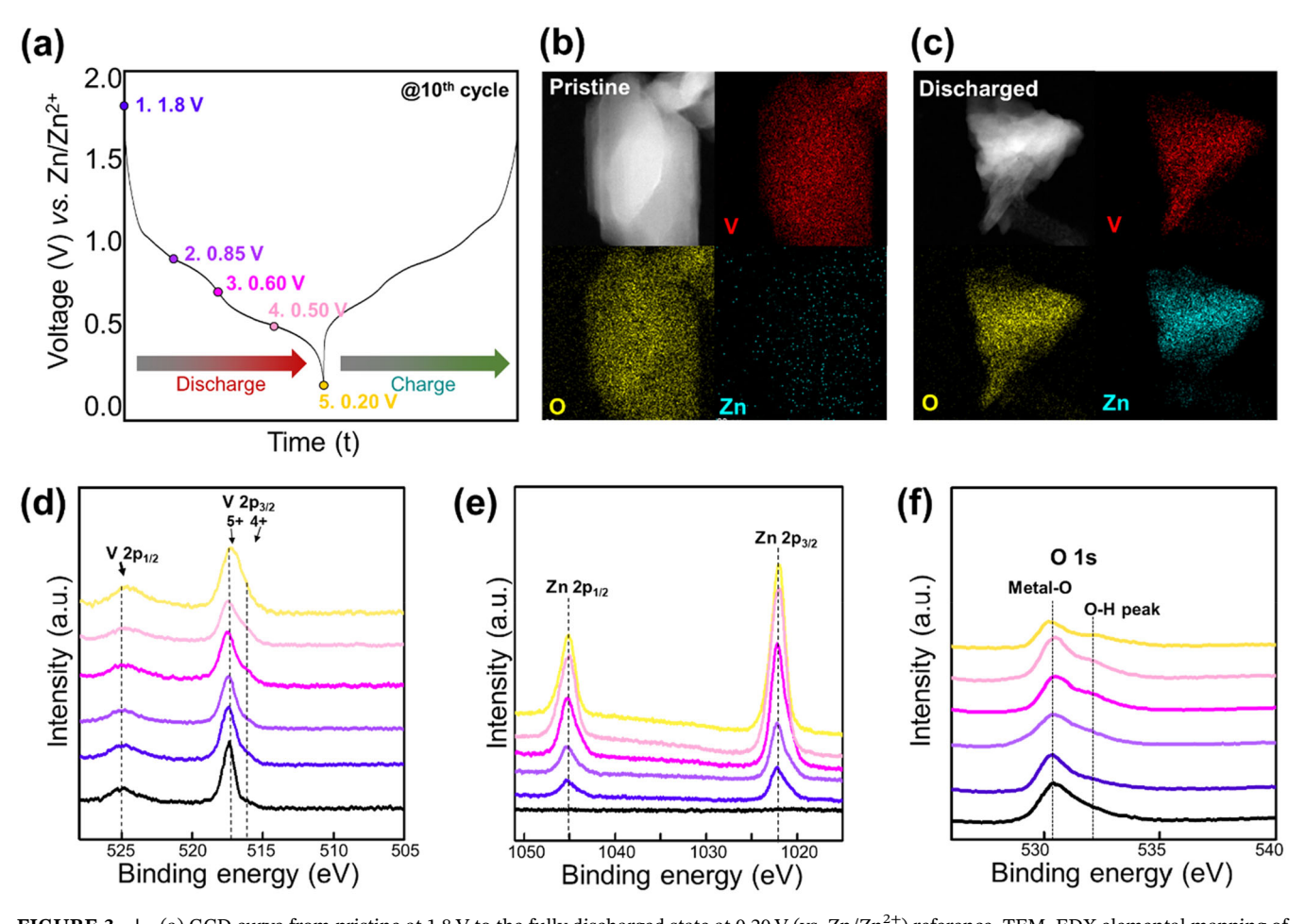


FIGURE 3 | (a) GCD curve from pristine at 1.8 V to the fully discharged state at $0.20 \,\mathrm{V}$ (vs. $\mathrm{Zn/Zn^{2+}}$) reference. TEM-EDX elemental mapping of (b) pristine and (c) fully discharged $\mathrm{V_2O_{4.86}}$. XPS spectra of (d) V 2p, (e) Zn 2p, and (f) O 1s.

underscoring their strong electrochemical durability. As shown in Figure 2e, electrochemical impedance spectroscopy (EIS) was conducted to compare the interfacial and charge transport properties of high-crystalline V_2O_5 and low-crystalline $V_2O_{4.86}$ before and after cycling. Initially, the interfacial resistance ($R_{\rm IR}$) values were 2.01 Ω for high-crystalline V_2O_5 and 2.55 Ω for low-crystalline $V_2O_{4.86}$. After 700 cycles, these values slightly increased to 2.74 Ω ($V_2O_{4.86}$) and 3.35 Ω (V_2O_5), respectively. This suggests that the high-crystalline V_2O_5 exhibits lower initial interfacial resistance but experiences a more pronounced increase during cycling, likely due to greater structural strain and volume changes.

Regarding the charge transfer resistance (R_{ct}), the low-crystalline $V_2O_{4.86}$ showed an increase from $3.2\,\Omega$ to $27\,\Omega$ after cycling. In comparison, the high-crystalline V_2O_5 exhibited a more significant rise, reaching $40\,\Omega$, indicating the formation of interfacial by-products or passivation layers that may hinder charge transfer by partially blocking the electrode surface. The Warburg slope of high-crystalline V_2O_5 was consistently lower than that of low-crystalline $V_2O_{4.86}$, implying more sluggish Zn^{2+} diffusion in the former. Moreover, a further degradation of the slope was observed after cycling, indicating a decline in diffusion kinetics due to structural degradation.

To further elucidate the charge storage mechanism of the low-crystalline $\rm V_2O_{4.86}$ cathode, CV measurements were performed at scan rates ranging from 0.2 to 1.0 mV s $^{-1}$ (Figure 2f). Power-law analysis was applied to distinguish between surface-limited capacitive behavior and diffusion-controlled kinetics. The power-law coefficients (b-values) for the two reduction processes were calculated as 0.9527 at 0.9 V and 0.9013 at 0.5 V (Figure 2g). These values indicated a significant contribution from capacitive reactions, suggesting that surface-limited processes modulate the overall charge storage capacity.

Further analysis revealed that ~29.9% of the zinc and/or proton ions participated in diffusion-controlled reactions with $\rm V_2O_5$, as determined from the ratio of capacitive and diffusion-controlled contributions (Figure 2h and Figure S11). These findings highlight the dual contribution of surface capacitive reactions with small bulk diffusion mechanisms to the charge storage in low-crystalline $\rm V_2O_{4.86}$, indicating that these surface redox reactions may attribute to higher fast charge–discharge properties.

3.3 | Charge Storage Mechanism of Low-Crystalline V₂O_{4,86}

Figure 3 presents the elemental analysis of the low-crystalline $V_2O_{4.86}$ cathode during the discharge-charge cycle. The GCD profile highlighted the electrode's behavior from the pristine state at $1.8 \, \text{V}$ (vs. Zn/Zn^{2+}) to the fully discharged state at $0.20 \, \text{V}$ (vs. Zn/Zn^{2+}) (Figure 3a).

Elemental mapping of the pristine electrode (Figure 3b) revealed a uniform distribution of vanadium and oxygen atoms, with no detectable zinc atoms present. Upon full discharge (Figure 3c), the electrode showed a uniform distribution of V, O, and Zn, indicating the incorporation of zinc ions into the vanadium oxide matrix during the discharge reaction. This

observation confirms the active involvement of zinc ions in the redox processes of the low-crystalline $\rm V_2O_{4.86}$ cathode, which contributes to its electrochemical performance.

X-ray photoelectron spectroscopy (XPS) analysis was conducted to investigate the chemical states of vanadium, zinc, and oxygen at different voltage states (Figure 3d-f). The V 2p spectrum (Figure 3d) showed three distinct peaks corresponding to V^{5+} and V^{4+} oxidation states: 525.0 eV (V^{5+} 2p_{1/2}), 517.5 eV $(V^{5+} 2p_{3/2})$, and 516.0 eV $(V^{4+} 2p_{3/2})$. These peaks are consistent with previously reported values and indicate the involvement of vanadium redox reaction in the electrochemical process [31]. The Zn 2p spectrum (Figure 3e) revealed an increase in the intensity of Zn 2p_{1/2} and Zn 2p_{3/2} peaks during the discharge process, confirming the intercalation of zinc ions into the V₂O₅ structure and their active participation in redox reactions. The O 1s spectrum (Figure 3f) showed the presence of signals across all voltage states, with an observed increase in the O-H peak intensity during discharge. This increase is attributed to the formation of Zn₃(OH)₂VO₇·2(H₂O), indicating structural changes associated with the incorporation of Zn ions and water/ proton molecules with cathode.

To investigate the structural evolution of low-crystalline $V_2O_{4.86}$ during discharge, ex situ XRD analysis was conducted at specific voltages of 0.2, 0.5, 0.6, 0.85, and 1.8 V (Figure 4a). During the wetting process, the low-crystalline $V_2O_{4.86}$ was completely transformed into a new phase, which remained stable throughout the discharge process from 1.8 to 0.2 V. This newly formed phase has been extensively reported in previous studies and is identified as the $Zn_{3+x}(OH)_2V_2O_7\cdot 2(H_2O)$ structure [25–27]. Detailly, during the initial cycling, V_2O_5 undergoes a structural transformation upon reaction with Zn^{2+} , forming $Zn_{3+x}(OH)_2V_2O_7\cdot 2H_2O$, which subsequently acts as the active host structure. In general, $Zn_4(OH)_6(SO_4)\cdot nH_2O$ side product from electrolyte, which is often observed as a surface byproduct due to proton insertion at lower potentials, is not observed in this first cycle.

In addition, we performed postdischarge TEM analysis (Figure S12) revealed that the highly crystalline V_2O_5 partially transformed into $Zn_{3+x}(OH)_2V_2O_7\cdot 2H_2O$, with the original phase still observable, likely due to the slower conversion kinetics associated with its larger particle size. On the other hand, the low-crystalline $V_2O_{4.86}$ underwent a more complete and rapid phase transformation, which can be attributed to its smaller particle size and the unstable amorphous structure.

To further investigate the structural reversibility upon charging, ex situ XRD measurements were performed during the charging process. The corresponding patterns (Figure S13) reveal no recovery to the initial phase ($V_2O_{4.86}$), indicating that reversible zinc ion intercalation occurs with the $Zn_{3+x}(OH)_2V_2O_7\cdot 2H_2O$ phase.

The stability of the $Zn_{3+x}(OH)_2V_2O_7\cdot 2(H_2O)$ phase during cycling underscores its suitability as a robust host structure for zinc-ion intercalation. The initial wetting process acts as an activation step, stabilizing the material's electrochemical performance, as illustrated in the reaction schematic (Figure 4b). In this process, the α - V_2O_5 phase transforms through

6 of 9 Battery Energy, 2025

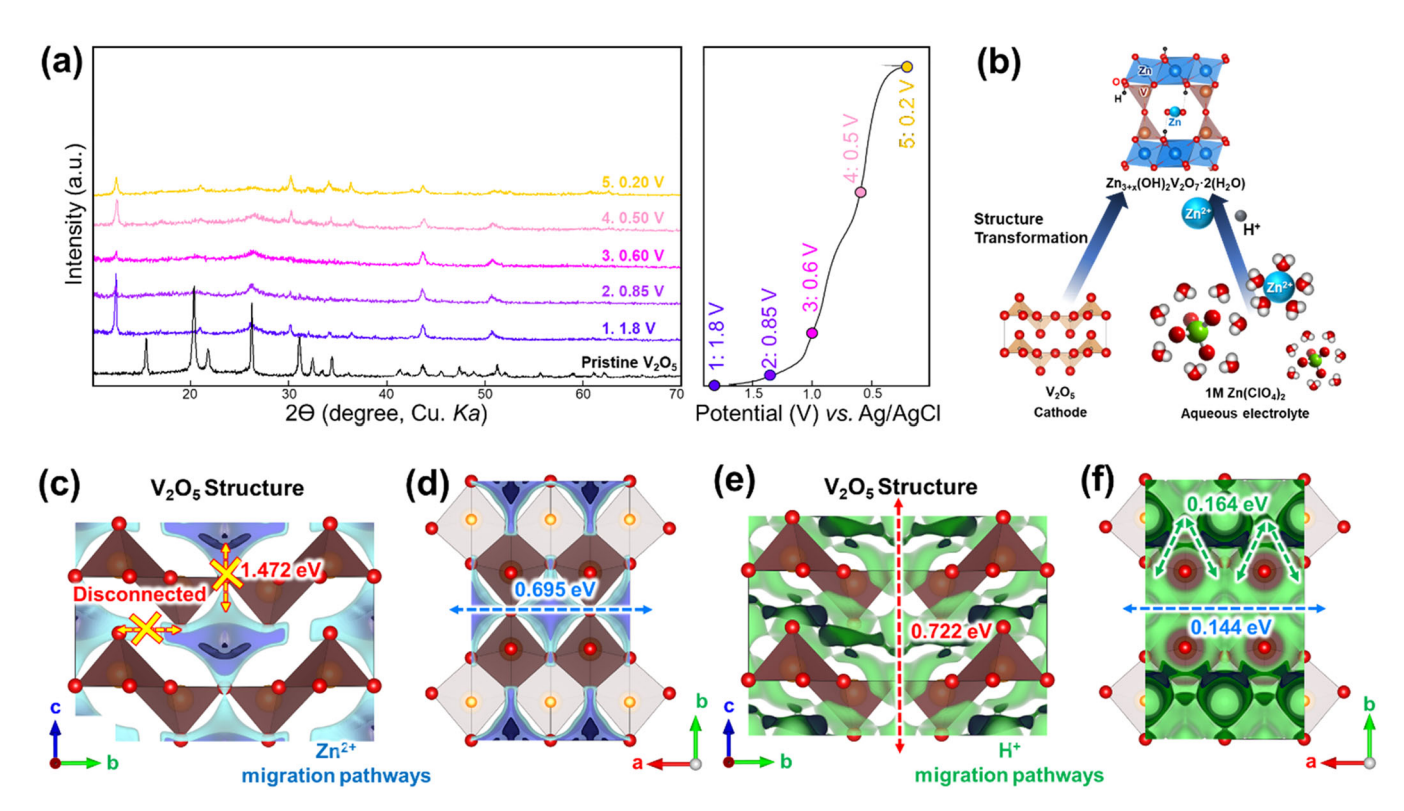


FIGURE 4 | (a) XRD peak analysis of $V_2O_{4.86}$ at various discharge voltages and in its pristine state, correlated with the GCD profile. (b) Schematic representation of the structural transformation mechanism resulting from the reaction between V_2O_5 and 1 M Zn(ClO₄)₂. (c and d) Migration pathways and bond strength comparison in high-crystalline V_2O_5 . (e and f) Migration pathways and bond strength in low-crystalline $V_2O_{4.86}$.

interactions with zinc ions and protons, forming the stable $Zn_{3+2}(OH)_2V_2O_7\cdot 2(H_2O)$ structure. To further analyze the activity and ionic pathways of the low-crystalline V₂O_{4.86} structure, bond valence sum (BVS) calculations were conducted [29, 30]. The zinc migration pathways and energy barriers are shown in Figure 4c-f. In high-crystalline V₂O₅, zinc diffusion was largely restricted to the a-axis (Figure 4c,d) due to a high activation energy barrier of 1.472 eV along the c-axis, limiting its electrochemical activity. Only one-dimensional diffusion along the a-axis was possible, with a lower activation barrier of 0.695 eV. In contrast, lowcrystalline V₂O_{4.86}, with oxygen vacancies, exhibited significantly improved zinc-ion mobility (Figure 4e,f). The weakened bonding, resulting from structural defects, reduced migration barriers to 0.722 eV in the b-c plane and 0.144/0.164 eV in the a-b plane, enabling multidimensional diffusion pathways. These additional pathways allow for more efficient zinc-ion intercalation, resulting in improved electrochemical activity. Thus, the highly active and defect-rich structure of low-crystalline V₂O_{4,86} not only facilitates better zinc-ion transport but also supports the phase transformation to Zn_{3+x}(OH)₂V₂O₇·2(H₂O), as confirmed by our earlier electrochemical data. This synergy between structural engineering and electrochemical performance highlights the advantages of oxygen-vacancy-rich V₂O_{4.86} for ZIB applications.

Figure 5a illustrates the overall reaction mechanism of V_2O_5 during its structural transformation and redox reactions. Initially, the α - V_2O_5 structure underwent a phase transformation into the $Zn_{3+x}(OH)_2V_2O_7\cdot 2(H_2O)$ phase during the wetting process or reduction–oxidation cycling. This newly formed $Zn_{3+x}(OH)_2V_2O_7\cdot 2(H_2O)$ structure then acted as a stabilized host for Zn^{2+} and proton intercalation and extraction,

enabling reversible operation in ZIBs. The stabilized Zn_{3+x}(OH)₂V₂O₇·2(H₂O) structure demonstrated excellent adaptability and durability as a host. Despite extensive research on the electrochemical properties of V2O5 and Zn_{3+x}(OH)₂V₂O₇·2(H₂O), the underlying storage mechanism for zinc and proton ions remains unclear to date. To address this, we calculated the zinc migration pathways and energy barriers within the Zn_{3+x}(OH)₂V₂O₇·2(H₂O) structure, as shown in Figure 5b. The results revealed a high migration barrier for zinc ions (1.197 eV), suggesting that the transformation of V₂O₅ to $Zn_{3+x}(OH)_2V_2O_7\cdot 2(H_2O)$ is accompanied by zinc ion intercalation. However, once the structure was stabilized as Zn_{3+x}(OH)₂V₂O₇·2(H₂O), zinc ions faced significant difficulty in diffusing further, limiting their role in subsequent charge storage. To investigate the alternative contribution of protons, we performed proton diffusion calculations within the $Zn_{3+x}(OH)_2V_2O_7\cdot 2(H_2O)$ structure (Figure 5c). The results demonstrated highly active proton diffusion, characterized by a significantly lower migration barrier of 0.439 eV. This indicates that, after the structural transformation, protons predominantly contribute to the charge storage mechanism within $Zn_{3+x}(OH)_2V_2O_7\cdot 2(H_2O)$.

These findings highlight a dual mechanism during the cycling process: an initial zinc-ion-driven structural transformation of V_2O_5 into $Zn_{3+x}(OH)_2V_2O_7\cdot 2(H_2O)$, followed by proton-driven charge storage in the transformed structure. Additionally, the low-crystalline oxygen vacancy in $V_2O_{4.86}$ leads to fast structural transformation. These results provide deeper insights into the roles of complex zinc ions and protons in the electrochemical performance of ZIBs.

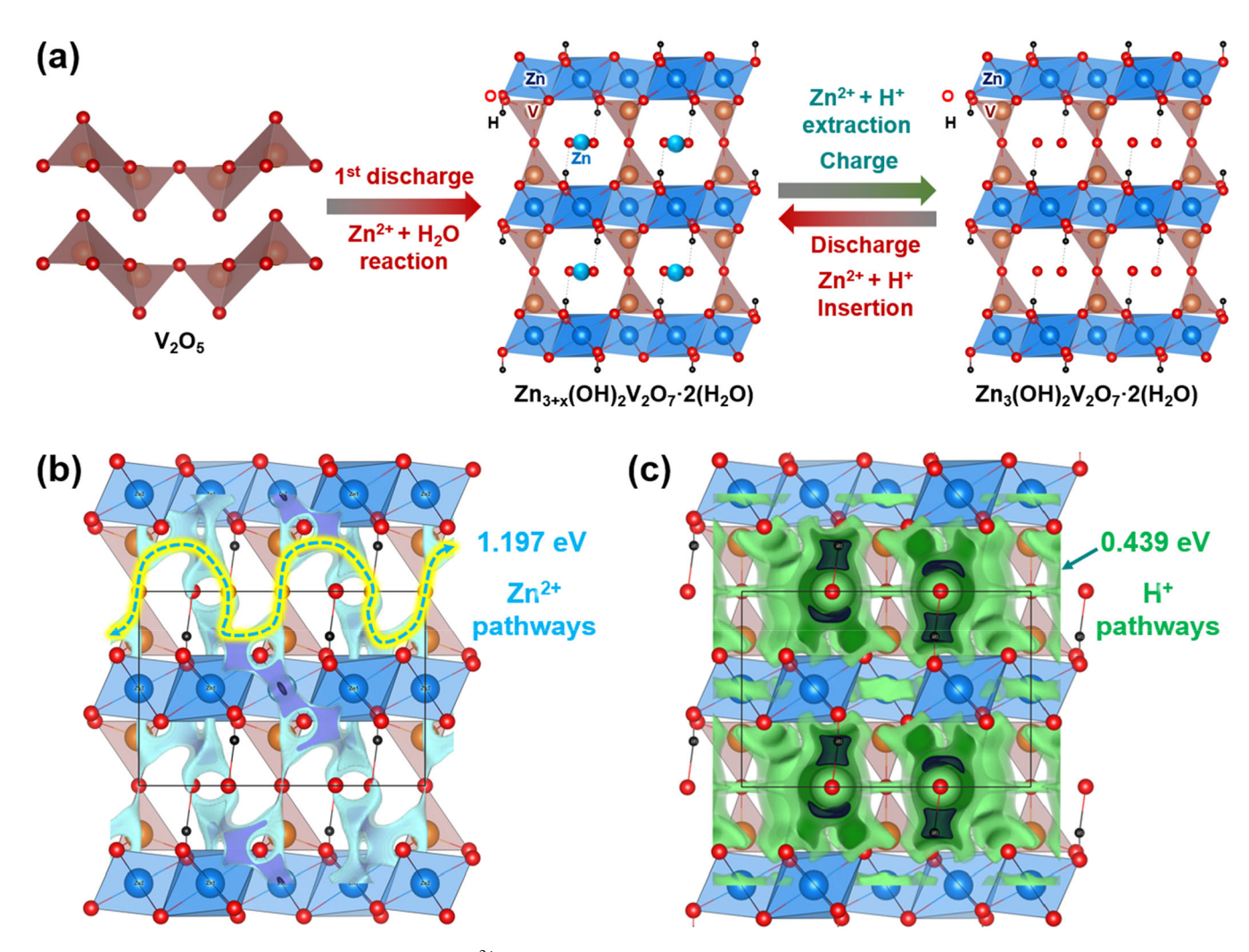


FIGURE 5 | (a) Schematic representation of the Zn^{2+} insertion and extraction processes during the charge/discharge reactions of V_2O_5 . (b) One-dimensional Zn ion diffusion pathways and migration barriers in the $Zn_{3+x}(OH)_2V_2O_7\cdot 2(H_2O)$ structure. (c) Two-dimensional proton diffusion pathways and migration barriers in the $Zn_{3+x}(OH)_2V_2O_7\cdot 2(H_2O)$ structure.

4 | Conclusion

This study underscores the transformative potential of low-crystalline vanadium oxide ($V_2O_{4.86}$) cathodes with engineered oxygen vacancies in enhancing the performance of aqueous ZIBs. Electrochemical analyses demonstrated that low-crystalline $V_2O_{4.86}$ achieves a remarkable 22% improvement in capacity (360 vs. 295 mAh g $^{-1}$) at a current density of 0.1 A g $^{-1}$, accompanied by excellent rate capability and cycling durability. To elucidate the reaction mechanisms and the role of oxygen vacancies, comprehensive structural analyses, migration pathway mapping, and energy barrier calculations were conducted.

The presence of oxygen vacancies activated a shift from the original one-dimensional zinc-ion diffusion pathway to a two-dimensional pathway, significantly reducing the migration barrier. This modification enabled a rapid transformation of low-crystalline $V_2O_{4.86}$ into the $Zn_{3+x}(OH)_2V_2O_7\cdot 2(H_2O)$ phase, leading to improved electrochemical activity. Furthermore, in the transformed $Zn_{3+x}(OH)_2V_2O_7\cdot 2(H_2O)$ structure, proton reactions were higher than zinc-ion reactions, further boosting charge storage capabilities.

While the low-crystalline $V_2O_{4.86}$ cathode offers rapid structural activation and higher initial capacity, its cycling stability is limited due to severe vanadium dissolution. Since vanadium dissolution is a common issue in V-based cathodes, future research should focus on mitigating this challenge to enable stable long-term performance.

These findings provide crucial insights into the interplay between structural engineering and oxygen vacancy modulation in optimizing vanadium oxide cathodes for ZIBs. This study paves the way for the development of advanced cathode materials, offering a scalable approach to enhance the efficiency, performance, and sustainability of next-generation aqueous secondary batteries.

Acknowledgments

This work was partly supported by the Global Joint Research Program funded by Pukyong National University (202411790001) and JSPS KAKENHI Grant No. JP22K14726.

Conflicts of Interest

The authors declare no conflicts of interest.

8 of 9 Battery Energy, 2025

Data Availability Statement

The data that support the findings of this study are available from the corresponding author upon reasonable request.

References

- 1. M. Armand and J. M. Tarascon, "Building Better Batteries," *Nature* 451 (2008): 652–657.
- 2. S. K. Das, S. Mahapatra, and H. Lahan, "Aluminium-Ion Batteries: Developments and Challenges," *Journal of Materials Chemistry A* 5 (2017): 6347-6367.
- 3. M. E. Arroyo-de Dompablo, A. Ponrouch, P. Johansson, and M. R. Palacín, "Achievements, Challenges, and Prospects of Calcium Batteries," *Chemical Reviews* 120 (2019): 6331–6357.
- 4. M. S. Chae, D. Setiawan, H. J. Kim, and S. T. Hong, "Layered Iron Vanadate as a High-Capacity Cathode Material for Nonaqueous Calcium-Ion Batteries," *Batteries* 7, no. 3 (2021): 54.
- 5. D. Setiawan, H. Lee, H. Bu, D. Aurbach, S. T. Hong, and M. S. Chae, "Magnesium Ions Storage in Molybdenum Oxide Structures Examined as a Promising Cathode Material for Rechargeable Magnesium Batteries," *Small Structures* 5, no. 1 (2024): 2300228.
- 6. D. Aurbach, Z. Lu, A. Schechter, et al., "Prototype Systems for Rechargeable Magnesium Batteries," *Nature* 407, no. 6805 (2000): 724–727.
- 7. C. Xu, B. Li, H. Du, and F. Kang, "Energetic Zinc Ion Chemistry: The Rechargeable Zinc Ion Battery," *Angewandte Chemie International Edition* 51, no. 4 (2012): 933–935.
- 8. G. Bergman, N. Bruchiel-Spanier, O. Bluman, et al., "To What Extent Do Anions Affect the Electrodeposition of Zn?," *Journal of Materials Chemistry A* 12, no. 24 (2024): 14456–14466.
- 9. D. Setiawan, H. Lee, H. H. Kwak, S. T. Hong, and M. S. Chae, "Bi-Layered Calcium Vanadium Oxide as a Cathode Material for Wet Organic Electrolyte-Based Rechargeable Zn-Ion Batteries," *Journal of Energy Storage* 72 (2023): 108497.
- 10. H. Lee, A. Nimkar, H. Lee, et al., "New Mn Electrochemistry for Rechargeable Aqueous Batteries: Promising Directions Based on Preliminary Results," *Energy & Environmental Materials* 8 (2024): e12823.
- 11. H. Lee, A. Nimkar, N. Shpigel, et al., "π-Electron-Assisted Charge Storage in Fused-Ring Aromatic Carbonyl Electrodes for Aqueous Manganese-Ion Batteries," *ACS Energy Letters* 9, no. 11 (2024): 5627–5634.
- 12. H. Lee, H. Lee, J. Pyun, S. T. Hong, and M. S. Chae, "Monoclinic Silver Vanadate ($Ag_{0.33}V_2O_5$) as a High-Capacity Stable Cathode Material for Aqueous Manganese Batteries," *Advanced Science* 11, no. 39 (2024): 2406642.
- 13. Y. Shi, Y. Chen, L. Shi, et al., "An Overview and Future Perspectives of Rechargeable Zinc Batteries," *Small* 16, no. 23 (2020): 2000730.
- 14. K. W. Nam, H. Kim, J. H. Choi, and J. W. Choi, "Crystal Water for High Performance Layered Manganese Oxide Cathodes in Aqueous Rechargeable Zinc Batteries," *Energy & Environmental Science* 12, no. 6 (2019): 1999–2009.
- 15. B. Sambandam, V. Mathew, S. Kim, et al., "An Analysis of the Electrochemical Mechanism of Manganese Oxides in Aqueous Zinc Batteries," *Chem* 8, no. 4 (2022): 924–946.
- 16. L. Wu, Z. Li, Y. Xiang, et al., "Unraveling the Charge Storage Mechanism of β -MnO $_2$ in Aqueous Zinc Electrolytes," *ACS Energy Letters* 9 (2024): 5801–5809.
- 17. X. Li, Z. Chen, Y. Yang, S. Liang, B. Lu, and J. Zhou, "The Phosphate Cathodes for Aqueous Zinc-Ion Batteries," *Inorganic Chemistry Frontiers* 9, no. 16 (2022): 3986–3998.
- 18. D. Bin, Y. Du, B. Yang, et al., "Progress of Phosphate-Based Polyanion Cathodes for Aqueous Rechargeable Zinc Batteries," *Advanced Functional Materials* 33, no. 8 (2023): 2211765.

- 19. K. Zhu and W. Yang, "Vanadium-Based Cathodes for Aqueous Zinc-Ion Batteries: Mechanisms, Challenges, and Strategies," *Accounts of Chemical Research* 57, no. 19 (2024): 2887–2900.
- 20. F. Wan and Z. Niu, "Design Strategies for Vanadium-Based Aqueous Zinc-Ion Batteries," *Angewandte Chemie* 131, no. 46 (2019): 16508–16517.
- 21. H. Pan, Y. Shao, P. Yan, et al., "Reversible Aqueous Zinc/Manganese Oxide Energy Storage From Conversion Reactions," *Nature Energy* 1 (2016): 16039.
- 22. M. Chen, S. C. Zhang, Z. G. Zou, et al., "Review of Vanadium-Based Oxide Cathodes as Aqueous Zinc-Ion Batteries," *Rare Metals* 42 (2023): 2868–2905.
- 23. W. Zhang, C. Zuo, C. Tang, et al., "The Current Developments and Perspectives of V₂O₅ as Cathode for Rechargeable Aqueous Zinc-Ion Batteries," *Energy Technology* 9, no. 2 (2021): 2000789.
- 24. X. Niu, N. Li, Y. Chen, et al., "Structure Evolution of V_2O_5 as Electrode Materials for Metal-Ion Batteries," *Batteries & Supercaps* 6, no. 9 (2023): e202300238.
- 25. K. Zhu, T. Wu, and K. Huang, "Understanding the Dissolution and Phase Transformation Mechanisms in Aqueous Zn/α - V_2O_5 Batteries," *Chemistry of Materials* 33, no. 11 (2021): 4089–4098.
- 26. X. Chen, L. Wang, H. Li, F. Cheng, and J. Chen, "Porous V_2O_5 Nanofibers as Cathode Materials for Rechargeable Aqueous Zinc-Ion Batteries," *Journal of Energy Chemistry* 38 (2019): 20–25.
- 27. S. Lee, W. Jin, S. H. Kim, et al., "Oxygen Vacancy Diffusion and Condensation in Lithium-Ion Battery Cathode Materials," *Angewandte Chemie International Edition* 58, no. 31 (2019): 10478–10485.
- 28. S. C. Lim, J. Lee, H. H. Kwak, et al., "Unraveling the Magnesium-Ion Intercalation Mechanism in Vanadium Pentoxide in a Wet Organic Electrolyte by Structural Determination," *Inorganic Chemistry* 56, no. 14 (2017): 7668–7678.
- 29. H. Chen, L. L. Wong, and S. Adams, "SoftBV—A Software Tool for Screening the Materials Genome of Inorganic Fast Ion Conductors," *Acta Crystallographica. Section B, Structural Science, Crystal Engineering and Materials* 75 (2019): 18–33.
- 30. H. Chen and S. Adams, "Bond Softness Sensitive Bond-Valence Parameters for Crystal Structure Plausibility Tests," *IUCrJ* 4 (2017): 614–625.
- 31. J. Mendialdua, R. Casanova, and Y. Barbaux, "XPS Studies of V_2O_5 , V_6O_{13} , VO_2 and V_2O_3 ," Journal of Electron Spectroscopy and Related Phenomena 71, no. 3 (1995): 249–261.

Supporting Information

Additional supporting information can be found online in the Supporting Information section.